Hydrogen embrittlement II. Analysis of hydrogen-enhanced decohesion across (111) planes in α-Fe

Ivaylo H. Katzarov[1,2] and Anthony T. Paxton[1]

[1]*Department of Physics, King's College London, Strand, London WC2R 2LS, United Kingdom*
[2]*Bulgarian Academy of Science, Institute of Metal Science, 67, Shipchenski prohod Str., 1574 Sofia, Bulgaria*

This is the second of two papers that present a theoretical analysis of the phenomenon of hydrogen embrittlement of α-Fe. We make contact between the thermodynamic-kinetic continuum and cohesive zone models and the quantum-mechanical magnetic tight-binding approximation to interatomic forces. We are able to solve a coupled set of equations using quantum mechanically obtained atomistic data to follow the decohesion process in time as traction is applied to a hydrogen charged crystal and decohesion occurs between two (111) crystal planes. This scheme will be readily extended from transgranular to intergranular failure, although the complexities of the trapping sites in the cohesive zone associated with a grain boundary will greatly complicate the calculation of the configurational energy. Hydrogen-enhanced decohesion postulated widely in the field has not yet been demonstrated experimentally, although our calculations find a reduction in the ideal cohesive strength as a result of dissolved hydrogen in α-Fe from 30 to 22 GPa. Because of the well-known steep and nonlinear relation between plastic and ideal elastic work of fracture, this represents a very significant reduction in toughness as a result of a hydrogen concentration of less than ten atomic parts per million.

I. INTRODUCTION

There are two most frequently called upon mechanisms of hydrogen embrittlement in iron and steel. These are hydrogen-enhanced localized plasticity (HELP), which is the subject of the first in this series of two papers [1], and hydrogen-enhanced decohesion (HEDE), which is the subject of this paper. Decohesion associates hydrogen embrittlement with a decrease in the atomic bond strength due to hydrogen segregation at a grain boundary or other interface. The impurity reduces the cohesive strength of interfaces, which leads to initiation and propagation of brittle cracks along these interfaces when the applied stress σ_{app} exceeds the cohesive strength σ_{coh}. High concentrations of hydrogen and the decohesion event could occur at a variety of locations [2]: (i) adsorbed hydrogen at crack tips, (ii) ahead of cracks where dislocation shielding effects result in a tensile-stress maximum, (iii) positions of maximum hydrostatic stress, and (iv) particle-matrix interfaces ahead of cracks. Hydrogen may be present in the bulk of the material and penetrate into interfaces upon application of an external load. Unlike the instance of HELP there has been little direct experimental evidence for the action of HEDE, although recently cleavage at subgrain boundaries and transgranular fracture was observed in a microalloy steel [3]. The present work reinforces this finding by focusing on the simplified and idealized example of the hydrogen-enhanced decohesion across two (111) crystal planes in magnetic bcc α-Fe. The effect of hydrogen is a large reduction in the ideal cleavage strength σ_{coh} from 30 to 22 GPa. Because the fracture toughness is a very steep and nonlinear function of the ideal cohesive strength [4], this means that a reduction by this amount may well amount to a ductile-to-brittle transition.

The fracture mode associated with HEDE is in contrast to the catastrophic failure taking place in intrinsically brittle materials. The crack propagation rate is presumably controlled by stress-driven diffusion of the hydrogen along the interface ahead of the crack tip. Without an external load, the hydrogen interfacial concentration is relatively low and the embrittling

effect is small. A study of this complex phenomenon should include several aspects, such as a mechanical description of the crack growth, thermodynamics of interfacial decohesion in the presence of impurity atoms, and stress-driven diffusion along an interface. The basic thermodynamic aspects of decohesion at segregated interfaces were laid down by Rice [5], Hirth and Rice [6], and later elaborated by Rice and Wang [7]. They analyzed the process of uniform separation along a plane interface under a uniform tensile stress applied normal to the interface. Their analysis was focused on two limiting cases: (i) "slow" separation in which diffusion of the impurity towards the interface is much faster than the separation and (ii) "fast" separation in which diffusion is so slow that the interface remains isolated from the impurity source and some segregation sites on the fracture surfaces remain empty after fracture. The first case is the limit of constant chemical potential μ, that is, equilibrium between the bulk and the interface; the second is the limit of constant composition and the resulting surfaces inherit whatever segregants were already present at the interface before fracture.

When hydrogen atoms are capable of migrating from the bulk to the crack tip and are trapped in the newly generated segregation sites, the mobile effect of hydrogen causes localized decohesion by further increasing the segregation in the cohesion zone, as illustrated in the cartoon of Fig. 1. In the stress free, equilibrium state, the cohesive zone is an atomically thin region—a grain boundary, or in our case, simply the space between two (111) crystal planes; and the occupancy of impurity θ is either the equilibrium segregated excess coverage Γ in the case of a grain boundary or essentially zero in the case of a perfect crystal. As traction is applied as indicated (σ in Fig. 1 is shorthand for σ_{app}) and we allow the symmetry to break and the two (111) planes to separate, then trap sites appear which attract hydrogen from the surrounding bulk. If the hydrogen serves to weaken the atomic bonds within the cohesive zone, then the process is self-perpetuating, and is governed by the amount of applied stress (we apply dead-weight loading) and the rate of diffusion of hydrogen
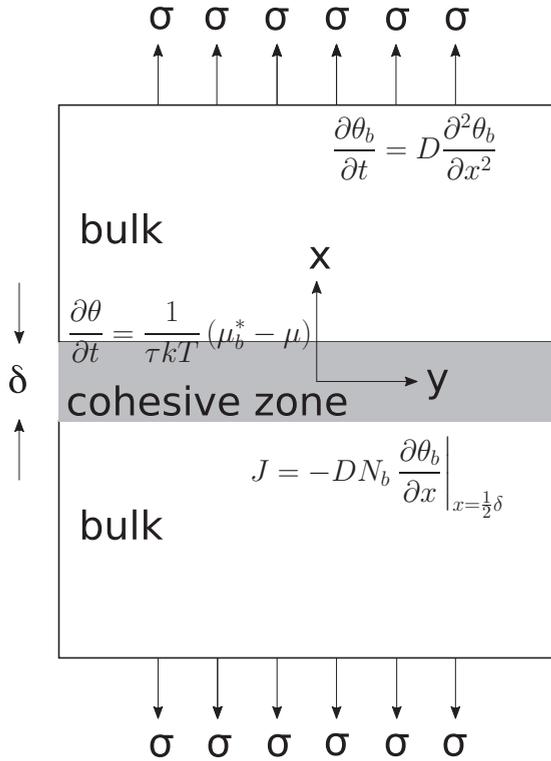
FIG. 1. Illustration of the cohesive zone (after Mishin *et al.* [9]), see the text for details.

from the bulk. The driving force for hydrogen exchange between the bulk and the cohesive zone is the difference in chemical potentials of hydrogen: μ in the cohesive zone and μ_b^* the chemical potential at the boundary, $x = \pm\delta$, of the bulk and the cohesive zone, Eq. (4), below. The width of the cohesive zone δ plays the role of a local crack opening displacement if we translate this model into the problem of a running crack cohesion zone analysis [8].

A reduction in the intergranular cohesive energy of an α-Fe $\Sigma = 3$ (111) grain boundary by hydrogen segregation was studied by first-principles calculations in Refs. [10–12]. Those studies did not investigate the role of hydrogen mobility. More detailed first-principles studies [13,14] on the effect of segregated hydrogen on grain boundary decohesion in α-Fe indicate that mobile hydrogen atoms play a more significant role on intergranular slow cracking (decohesion) than immobile hydrogen. To derive the effect of hydrogen segregation in the cohesive zone under transient conditions, one needs to know the chemical potential in the cohesive zone $\mu = \mu(\theta)$ as a function of the hydrogen occupancy, θ, of trap sites in the cohesive zone, which itself is a function of the separation processing time. The separation trajectory $\mu(\theta)$ is governed by the kinetics of transport of segregant from the bulk to the pair of separating fracture surfaces. Thermodynamic and kinetic models for the change in cohesion induced by segregation were proposed by Wang [15], who assumed a linear relation between chemical potential and hydrogen concentration in the cohesive zone; and by Van der Ven and Ceder [16] who adopted a constant-μ condition. Both models also show that a mobile segregant reduces the cohesion more strongly than an immobile segregant does.

To extend our effort to quantify the hydrogen effect on cohesive energy under various bulk hydrogen contents and temperatures, it is of importance to incorporate the hydrogen mobility and segregation energy in the cohesion zone. Mishin *et al.* [9] proposed an extension of the analysis of Hirth and Rice [6] to intermediate situations in between the limits of constant composition and constant chemical potential, in which the rates of separation and diffusion are comparable to one another. In their analysis of the kinetics of hydrogen supply to the interface, which is controlled by bulk diffusion, they postulate local thermodynamic equilibrium conditions at the bulk-interface boundary. In the present paper, we use the thermodynamic model proposed in Ref. [9] to study the process of uniform separation under a tensile stress along a (111) plane in α-Fe with different hydrogen concentrations in the bulk of the material. In our analysis, the local thermodynamic equilibrium conditions between the interface and the environment are upset. We assume that the hydrogen exchange at the bulk–interface boundary is controlled by a driving force proportional to the difference between chemical potentials in the bulk and in the cohesive zone. This results in a time-dependent interfacial hydrogen concentration that depends on the relation between the strain rate and the rate of bulk diffusion. When decohesion occurs, the hydrogen concentration between the separating atomic planes could be quite large, sometimes attaining saturation levels. A difference in hydrogen concentration between the bulk and the decohering region locally modifies the mechanical response of the solid, altering the mechanisms and rates of crack growth from what it would be in the absence of impurities.

The organization of the paper is as follows. In Sec. II, we describe the continuum decohesion model as first introduced by Rice, Hirth, and Wang [5–7] and extended by Mishin *et al.* [9]. In Sec. III following Van der Ven and Ceder [16], we describe how the connection is made between the continuum model and atomistic scale as represented by the cohesion zone. Section III is separated into three parts: in Sec. III A, we focus on pure α-Fe, in Sec. III B, we describe how we include hydrogen in the bulk and in the cohesive zone, and in Sec. III C, we describe how we calculate the chemical potential in the cohesive zone. Section IV contains our results and discussion and we conclude in Sec. V.

II. CONTINUUM DECOHESION MODEL

We follow Mishin *et al.* [9] and we imagine a perfect crystal and choose a crystallographic plane across which we will separate the crystal into two halves. This is a simplification compared to the original work in which the plane was taken to be a grain boundary and the crystal a bicrystal [9,16]. The geometry is sketched in Fig. 1, while Fig. 2 shows an atomic scale view of the cohesive zone. It is the purpose of the present paper to link these two scales using quantum-mechanical calculation. In equilibrium, the separation between the two halves is the equilibrium distance d_0 between the crystallographic planes. As a tensile stress σ_{app} is applied, we insist the two halves separate by introducing a crack opening displacement δ. This serves to separate the system into three regions: two pieces of bulk crystal which are at most elastically strained and a *cohesive zone* of thickness δ. In the problem at
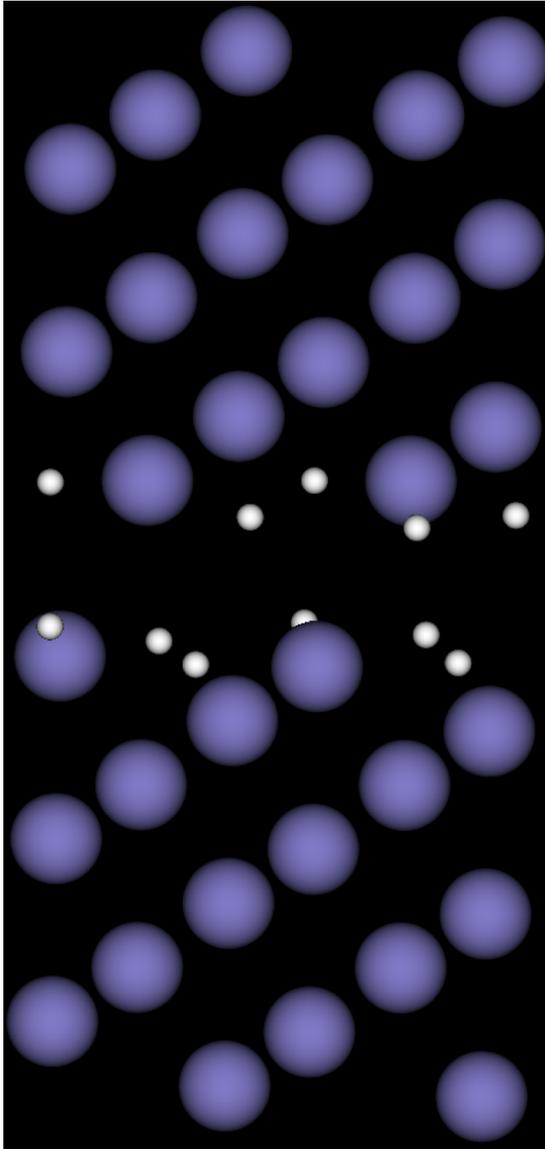
FIG. 2. An atomic scale view of the cohesive zone—snapshot from one of our simulations described in Sec. IV in which hydrogen atoms have segregated to the cohesive zone between two separating (111) crystal planes in magnetic α-Fe. Blue and white spheres represent iron and hydrogen atoms, respectively.

hand here, the crystal is pure α-Fe containing a nominal bulk concentration of hydrogen C_{H} usually expressed in atomic parts per million (appm). Since hydrogen occupies interstitial tetrahedral sites in α-Fe we may take it that there are N_b such sites per unit volume of which a fraction θ_b are occupied. In the initial, equilibrium, state therefore $\delta = 0$ and there are $N_b\theta_b$ hydrogen atoms *per unit volume*. As traction is applied and the space between the two halves opens up, we expect the tetrahedral interstices in the cohesive zone to become expanded and distorted and that these will act as deeper trap sites than the bulk tetrahedral interstices. Therefore hydrogen will be attracted by diffusion into the cohesive zone giving rise to an increased occupancy. The number of trap sites *per unit area* is denoted N and the fraction of those that are occupied is θ. The number of trap sites per unit volume in the cohesive

zone is N/δ and hence there are $N\theta/\delta$ hydrogen atoms per unit volume in the cohesive zone, compared to $N_b\theta_b$ in the adjoining bulk.

At zero stress, we have $\theta = \theta_b$ and $\mu = \mu_b$, where μ_b and μ are the chemical potentials of hydrogen in the bulk and in the cohesive zone, respectively. We may regard the stress as being a state function of the concentration and size of the cohesive zone [6,9], which is expressed as a *traction curve*

$$\sigma = \sigma(\theta,\delta) \qquad (1)$$

and if we assume a quasiequilibrium state during the application of an increasing traction then

$$\mu = \mu(\theta,\delta). \qquad (2)$$

We will see later in Sec. III C by explicit calculation that it is a good assumption to neglect hydrogen-hydrogen interactions and use an ideal solution form for the chemical potential in the cohesive zone. In addition, in view of the very limited bulk solubility, we may write

$$\mu_b = \mu_0 + kT \ln\left(\frac{\theta_b}{1 - \theta_b}\right). \qquad (3)$$

As the stress is applied and δ increases, the equilibrium is disturbed and hydrogen atoms are exchanged between the bulk and the cohesive zone. We follow Mishin *et al.* [9] and assume that the rate of change of concentration in the cohesive zone is driven by the chemical potential difference and hence that

$$\frac{\partial \theta}{\partial t} = \frac{1}{\tau kT}(\mu_b^* - \mu). \qquad (4)$$

Here, τ is a characteristic relaxation time, and μ_b^* is the chemical potential of hydrogen at the interface between the cohesive zone and the bulk, that is (see Fig. 1),

$$\mu_b^* = \mu_b(\theta_b^*); \quad \theta_b^* = \theta_b|_{x=\frac{1}{2}\delta}. \qquad (5)$$

Now, the rate of increase in number of hydrogen atoms per unit area of cohesive zone, $N\theta$, is equal to the sum of the two fluxes from above and below (Fig. 1),

$$N\frac{\partial \theta}{\partial t} = J_- - J_+, \qquad (6)$$

and each flux is expressed by Fick's first law as the product of the diffusivity D and the concentration gradients at $x = \pm\delta/2$,

$$J_+ = -DN_b\frac{\partial \theta_b}{\partial x}\bigg|_{x=\frac{1}{2}\delta}. \qquad (7)$$

Combination of (6) and (7) leads to

$$\frac{\partial \theta}{\partial t} = \frac{2DN_b}{N}\frac{\partial \theta_b}{\partial x}\bigg|_{x=\frac{1}{2}\delta}, \qquad (8)$$

and Fick's second law for hydrogen transport in the bulk reads

$$\frac{\partial \theta_b}{\partial t} = D\frac{\partial^2 \theta_b}{\partial x^2}, \qquad (9)$$

which completes the mathematical formulation of the problem. The coupled equations (1)–(5), (8), and (9) are solved numerically for different sets of external loads and bulk hydrogen concentrations. The procedure is as follows.

(1) The chosen applied stress σ_{app} leads to a crack opening displacement δ, which is read off the traction curve: one of the thin lines in Fig. 6 appropriate to the immediate value of the occupancy, θ, of hydrogen in the cohesive zone. At time zero, we have $\theta = \theta_b < 10^{-5}$ in view of the very low bulk concentration C_{H}. At the start of the simulations, we gradually increase the magnitude of the applied tensile load from zero until it reaches a constant value.

(2) Due to the increase in separation δ in step 1, there is a change in the chemical potential according to Eq. (2).

(3) As a result of the change in μ, there will be an exchange of hydrogen between the bulk and the cohesive zone, induced by the driving force, $\mu_b^* - \mu$, so in this step the occupancy θ is updated by a numerical integration of Eq. (4) over the interval Δt. It is here that the time constant τ plays a role.

(4) This, in turn leads to a change in the gradient boundary condition at the boundary, $x = \pm\delta/2$, between the bulk and the cohesive zone, which is calculated from Fick's first law (8).

(5) The new value furnishes us with a new boundary condition for the solution of Fick's second law (9), which we solve to generate a concentration profile of hydrogen in the bulk. Typical concentration profiles at $T = 300$ K are shown in Fig. 12. We use $D = 8.89 \times 10^{-9}$ m^2/s at 300 K and $D = 4.50 \times 10^{-9}$ m^2/s at 200 K [17].

(6) In the last step, in accordance with Eq. (3), the bulk hydrogen chemical potential is updated.

The steps 1–6 are repeated for successive time steps Δt. The choice of time constant τ does not affect the cohesive strength σ_{coh}, which is the maximum stress over the whole process, but it does affect the time to rupture.

III. COHESIVE ZONE MODEL

In order to proceed, it is necessary to make the connection between the continuum theory and the interatomic forces that are responsible for the cohesion (and decohesion) across the atomic planes, or indeed grain boundaries. As we see in Sec. III B, it is necessary to make a large number of calculations of total energy in a wide array of configurations (for example, Fig. 2) and the density functional theory is generally too costly for this, especially as in future work we wish to extend this formalism to grain boundary decohesion. Therefore we employ the magnetic tight-binding approximation to the DFT, which was introduced by Paxton, Finnis, and Elsässer [18,19]. For the calculations, here we use the slightly modified tight-binding model of Ref. [20].

A. Cohesive zone model in pure bcc Fe

In order to obtain the traction curve (1) we work with excess quantities: cohesive zone energy per unit area and elongation [16]. These excess quantities can be applied to situations where the crack is characterised by an extended region of gradual decohesion.

For the atomistic calculations, we use "supercells" such as illustrated in Fig. 2, for which periodic boundary conditions are applied in all three directions. The excess energy is defined

as [16]

$$e(\sigma) = \frac{E_{\mathrm{tot}}(\sigma)}{A} - (n_p - 1)E_{\mathrm{el}}(\sigma) \tag{10}$$

in which E_{tot} is the total energy of the supercell at a stress σ, A is the area projected onto the cohesive zone, and E_{el} is the elastic energy per unit area, per plane of atoms of an equivalent supercell that is homogeneously stretched at the same stress [16]. The total number of atomic planes in the supercell is n_p and (10) serves to illustrate that the excess energy in the case of the homogeneously deformed supercell is just the elastic energy associated with one crystal plane, so that as the two halves in Fig. 1 are decoupled, (10) is the excess energy associated with the cohesive zone only. In a similar way, we can define the excess length [16]

$$l(\sigma) = L(\sigma) - (n_p - 1)L_{\mathrm{el}}(\sigma),$$

where $L(\sigma)$ is the length of the supercell at stress σ and L_{el} is the separation of the crystal planes in a homogeneously elongated supercell at the same stress. The crack opening or width of the cohesive zone is hence

$$\delta(\sigma) = l(\sigma) - d_0.$$

Using the magnetic tight-binding approximation [20], we calculate E_{tot} and E_{el} for a range of lengths of a supercell containing 16 (111) planes. A vacuum region is introduced above and below the slab of atoms in order to allow relaxation of the size of the cohesive zone. We then fit our data to a universal binding energy curve [21]

$$e(\delta) = e_0 - 2\gamma \left(1 + \frac{\delta}{\lambda}\right) \exp\left(-\frac{\delta}{\lambda}\right) \tag{11}$$

in order to have an analytic expression for convenience. The traction curve $\sigma(\delta)$ for pure α-Fe is the derivative of (11) with respect to δ.

We should point out, for clarity, that two locally stable states of deformation exist as the crystal is elongated perpendicular to the separating planes: (i) the crystal is homogeneously and elastically deformed (for small elongations) and (ii) the elongation is largely concentrated between one pair of decohering planes (for large elongations). Both states can be locally stable at intermediate elongations. We calculate atomistically the energy of the uniformly elongated state and a decohered state at different elongations. In the calculations, the atoms within the supercell are relaxed to minimise the energy of the cell. Periodic boundary conditions are used in all three directions, which requires introduction of a vacuum region above and below the slab of atoms in order to provide correct relaxation of the cohesive zone. To derive the excess variables, the data from the energy calculations of both states are substituted into Eq. (10) for the excess energy.

B. Cohesive zone model in the presence of hydrogen

The greatest complication in extending the cohesive zone model to include the effects of interstitial impurities arises from the fact that as the cohesive zone widens under traction, the binding energy for hydrogen at the trap sites becomes dependent on the crack opening or separation. We may simplify the situation somewhat by assuming that the number

of trap sites per unit area does not change, but that these evolve in a one-to-one manner from the originating bulk tetrahedral sites that existed between the two separating crystal planes in equilibrium. We use a lattice model from statistical mechanics to deduce the occupancies, θ, in the separating cohesive zone [16,22,23].

First, it is necessary to identify the trap sites and to calculate their binding energy. The latter quantity is calculated from 32 Fe atom supercells. Having identified trap sites for a given separation δ, we calculate the total energy, $E_{\text{tot}}(\text{Fe}_{32}\text{H}_n)$, of a supercell under stress having a number n of equivalent sites filled. Then the binding energy of these n hydrogen atoms in the cohesive zone is

$$E_{\text{bind}}(n) = E_{\text{tot}}(\text{Fe}_{32}\text{H}_n) - E_{\text{tot}}(\text{Fe}_{32}) - \frac{n}{2}E_{\text{H}_2} - nE_{\text{dis}},$$

(12)

where $E_{\text{tot}}(\text{Fe}_{32})$ is the total energy of the unstrained pure α-Fe supercell; $E_{\text{H}_2} = -4.75$ eV and $E_{\text{dis}} = 0.273$ eV (in the tight-binding model [19]) is the *dissolution energy* [19,24], which is defined as the energy difference between a hydrogen atom in a relaxed tetrahedral interstice in α-Fe and one in a hydrogen molecule. In point of fact, $E_{\text{bind}}(n)$ is independent of E_{H_2} since the same term appears in the definition of E_{dis} and cancels out of (12).

The second task is to identify the positions and degeneracy of the trap sites in the cohesive zone. We find from atomistic simulations that with increasing separation between two (111) planes, the original tetrahedral interstices transform into distorted interstitial sites as shown in Fig. 2. The 12 original and degenerate interstices become three groups with four degenerate sites in each group. By degeneracy here we mean that the energy does not change if one hydrogen atom is interchanged between sites in a group. Furthermore, the sites in each group are all the same distance from the surface layer of iron atoms, although this distance is different for each group. The total energy also changes if a hydrogen atom is moved from one group to another. The binding energy is greatest for the groups whose sites are closest to the surface layer, which means that hydrogen atoms preferentially occupy the sites nearest to the surface. In this way, as hydrogen atoms are added into the cohesive zone they first occupy sites in the group closest to the surface, then sites in the group that is next nearest and finally they will occupy the third group. Only one hydrogen atom will occupy each site.

As in the case of pure iron in Sec. III A in order to obtain an analytic traction curve we fit our results to a binding curve as in Eq. (11). For example, Fig. 3 shows a fit to our calculations of the excess energy in the case that half of the twelve sites are occupied—that is, $\theta = 1/2$. The dependence of the energy on hydrogen concentration is described using a lattice model [16,23]. In this model the configuration of hydrogen atoms in the cohesive zone is specified by occupation variable, s_i, assigned to each trap site i, which is $+1$ or -1 depending upon whether or not the site is occupied. A particular configuration is fully specified by the collection of occupation variables, $\mathbf{s} = (s_1, s_2, \dots)$. Each of the parameters in (11) will depend upon the configuration $\mathbf{s}$ and we approximate these as follows:
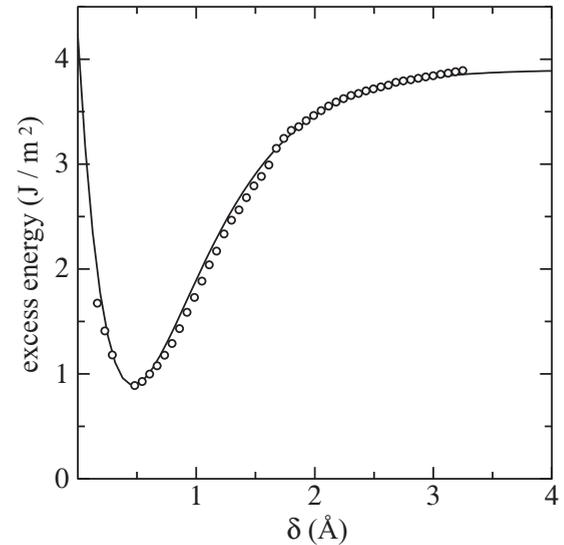
FIG. 3. Decohesion curve showing excess binding energy per unit area of cohesive zone as a function of opening displacement δ. The data points, calculated using the tight-binding approximation are fitted to the analytic binding form (11). The occupancy of hydrogen in the cohesive zone is one half. The zero of binding energy is the energy of the unstrained pure α-Fe supercell (see Fig. 5).

for any of the three variables, $\phi = e_0, \gamma$ or λ, we write [16]

$$\phi(\mathbf{s}) = \sum_i C_0^\phi + \sum_{k=1}^{3}\left(\sum_i C_{1,k}^\phi s_i + \frac{1}{2}\sum_{i,j} C_{2,k}^\phi s_i s_j \right). \quad (13)$$

The first sum is over all tetrahedral sites in the cohesive zone. In the second and third sums, i ranges over all lattice sites and j ranges over all neighboring sites to i in each of the clusters k of energetically equivalent sites. The coefficients, C_0^ϕ, $C_{1,k}^\phi$, and $C_{2,k}^\phi$, are independent of configuration in each cluster. For the hydrogen-iron system, the calculated closest hydrogen atom-pair interactions are small which justifies a short ranged lattice model. We obtain values for the coefficients C^ϕ in (13) by inversion using fitted parameters of the binding curves of distinct hydrogen configurations from the atomistic calculations. The parameters, $\gamma(\theta)$ and $\lambda(\theta)$, determined from the lattice model as functions of the hydrogen concentration are shown in Fig. 4. Energy versus separation curves for fixed hydrogen concentrations between decohering (111) planes (shown for intervals of 0.08 in occupancy) are illustrated in Fig. 5. The configuration dependence of the stress can also be parameterised within the cluster expansion (13). The stress dependence on separation and hydrogen configurations is the derivative of configurational energy

$$e(\theta, \delta) = e_0(\theta) - 2\gamma(\theta)\left(1 + \frac{\delta}{\lambda(\theta)}\right)\exp\left(-\frac{\delta}{\lambda(\theta)}\right) \quad (14)$$

with respect to the separation δ, since [16]

$$\sigma = \left(\frac{\partial e}{\partial \delta}\right)_{T,\theta}. \quad (15)$$

Figure 6 shows a family of traction curves (1) calculated at fixed values of the occupancy, θ, of hydrogen in the trap sites

FIG. 4. Values of the parameters of the binding curve, $\gamma(\theta)$ and $\lambda(\theta)$ as determined from the lattice model as functions of the occupancy θ of the trap sites in the cohesive zone.

in the cohesive zone. These curves are calculated by making magnetic tight-binding calculations of the relaxed structure and excess energy of slabs having a fixed value of separation δ, across the cohesive zone and a fixed occupancy θ. To achieve a particular value of δ, we apply an elongation to the supercell which we adjust until we obtain our target δ in the relaxed structure. Except at very small elongations, the total energy of two separated slabs is lower than the total energy of the uniformly, elastically strained slab [16]. Once we have fitted
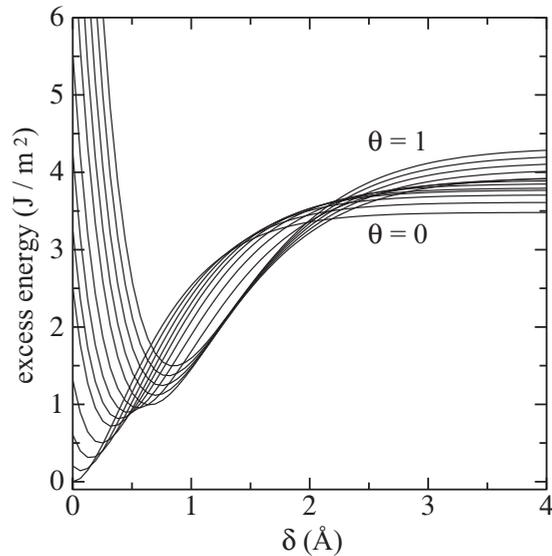
FIG. 5. Excess binding energy per unit area of cohesive zone as a function of opening δ between decohering (111) planes. Curves are shown at intervals $\Delta\theta = 0.08$ between $\theta = 0$ and 1 (zero to full occupancy of the trap sites in the cohesive zone). Note that the minimum in the $\theta = 0$ curve is at $\delta = 0$ as expected. As θ increases, this minimum moves to large values of δ as the presence of hydrogen has the effect of "jacking open" the two (111) planes.
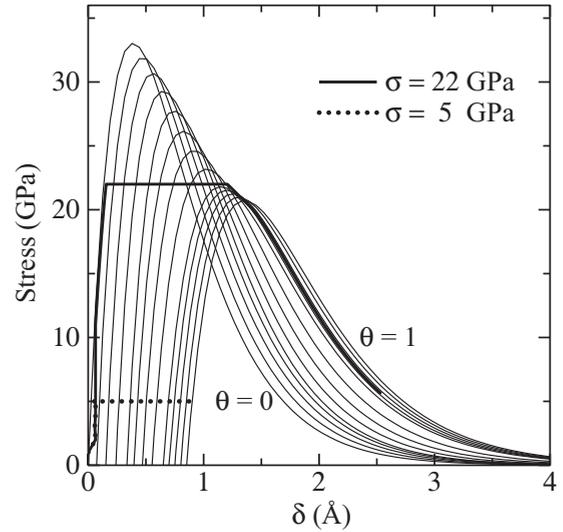
FIG. 6. Traction curves: stress σ, Eq. (15), as a function of opening δ. Each of the thin lines is one of a family of traction curves belonging to a particular value of the occupancy θ of hydrogen in the trap sites of the cohesive zone. Hence the curve with the largest peak stress, labeled $\theta = 0$, is the traction curve for pure α-Fe; while the curve labeled $\theta = 1$ is the traction curve if all the sites in the cohesive zone are occupied. The curves in between these belong to values of θ that are incremented in steps of 0.08. The maximum of each curve may be identified as a *critical stress for rupture* σ_{crit}. The thick solid and dotted lines are traction curves at fixed bulk hydrogen concentration, $C_H = 1$ appm, and fixed applied stress σ_{app}, see Sec. IV for a discussion of these two curves.

the binding curve (14) as in Fig. 3, we can obtain the stress by differentiation and plot curves as in Fig. 6.

C. Chemical potential in the cohesive zone

In order to "close the loop" and calculate a traction curve (1) the final task is to find the chemical potential (2) in the cohesive zone as a function of the occupancy θ and width δ of the cohesive zone (and also the bulk hydrogen concentration, C_H). To do this, we require statistical mechanics techniques which will take appropriate averages over the distinguishable configurations of hydrogen atoms between the decohering planes. Once the partition function Z is found then the chemical potential (2) is

$$\mu(\theta,\delta) = -kT \frac{\partial \ln Z(\theta,\delta)}{\partial \theta}. \quad (16)$$

To obtain the partition function, we employ the Wang-Landau Monte Carlo method [25], which estimates the density of states $g(E)$ via a random walk in energy space with a probability proportional to the reciprocal of the density of states. This is accomplished by modifying the estimated density of states to produce a "flat" histogram for the energy distribution. At the beginning of the random walk, the density of states is set for all energies E to $g(E) = 1$. Then we begin our random walk in energy space by flipping randomly the positions of the hydrogen atoms for different concentrations and separations in the cohesive zone. If E_1 and E_2 are energies before and after flipping, the transition probability from energy level E_1 to E_2

is

$$p(E_1 \rightarrow E_2) = \min\left[\frac{g(E_1)}{g(E_2)}, 1\right].$$

Each time an energy level E is visited, the corresponding density of states is updated by multiplying the existing value by a modification factor f. We keep walking randomly in energy space and modifying the density of states until the accumulated histogram $H(E)$ is "flat." At this stage, the estimated density of states converges to the true value with an accuracy proportion to $\ln f$. We then reduce the modification factor to a finer one and begin the next level random walk with the smaller modification factor f_1. The simulation process stops when the modification factor is smaller than a predefined final value.

Then the partition function can be derived at each temperature from the density of states via

$$Z(\theta, \delta) = \int g(e) \exp\left(-\frac{e(\theta, \delta)}{kT}\right) de. \tag{17}$$

However, use of an analytic expression for the chemical potential in the cohesive zone as a function of hydrogen concentration and separation in the nonlinear system of differential equations (1)–(5), (8), and (9) is highly advantageous. Such an analytic expression is furnished by an ideal solution model [16]

$$\mu(\theta, \delta) = \left(\frac{\partial e(\theta, \delta)}{\partial \theta}\right)_\delta + kT \ln\left(\frac{\theta}{1-\theta}\right). \tag{18}$$

Using the configurational energy (14), we have calculated the chemical potential in the cohesive zone for different separations δ and hydrogen concentrations θ, using both Wang-Landau Monte Carlo and the ideal solution model. The comparison shows excellent coincidence between the two methods (Fig. 7).

In fact for the hydrogen-iron system, we find that the ideal solution approximation yields essentially the same results as more accurate Wang-Landau Monte Carlo simulations. This indicates weak interaction between hydrogen atoms between decohering (111) planes and thereby justifies employment of the less expensive ideal solution model (18) to calculate chemical potential in the cohesive zone for different hydrogen concentrations and separations.

We must point out that the combination of the cluster expansion (13) with the Wang-Landau Monte Carlo approach and mean-field approximation within each of the groups of hydrogen atoms does amount to an approximation in our partition function (17). However, it brings two benefits: (i) it allows us to keep the number of expensive total energy calculations to a minimum and (ii) it furnishes us with an analytic expression for the chemical potential (18).

IV. RESULTS AND DISCUSSION

Now that we have a closed set of equations, with parameters determined from magnetic tight-binding calculations, solutions can be found for the decohesion process in real time. We begin with an equilibrium slab of α-Fe and choose an applied tensile stress σ_{app} and a nominal bulk concentration of hydrogen, C_H. Typical values in industrial practice and in the laboratory charging of specimens are, respectively, $C_H = 0.1$
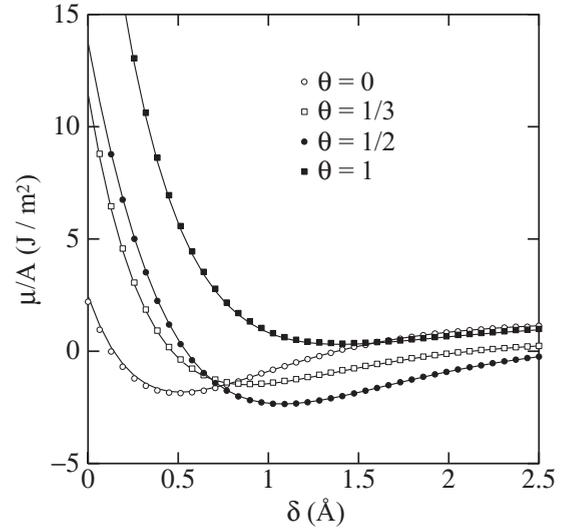
FIG. 7. Chemical potential μ divided by area A, projected by the cohesive zone, vs opening δ for four fixed values of occupancy θ of hydrogen in the cohesive zone. The solid curves show results from using the "exact" statistical mechanical Wang-Landau Monte Carlo and the points show the same quantities obtained from the ideal solution model (18). For completeness we should point out that strictly the chemical potential diverges at $\theta = 1$ and 0, therefore curves thus labeled are in fact calculated at $\theta = 1 - \epsilon$ and ϵ, where $\epsilon = 10^{-6}$.

and 10 appm. In the present work, three values are used: 0.1, 1, and 10 appm. We also choose as input a value of the time constant τ, that enters Eq. (4). We have used three values, namely, 10^{-10}, 10^{-5}, and 1 s. We also choose a suitable time step, $\Delta t = 10^{-5}\tau$.

We illustrate the progress of the steps listed at the end of Sec. II in Figs. 8 and 9, which show the evolution of the
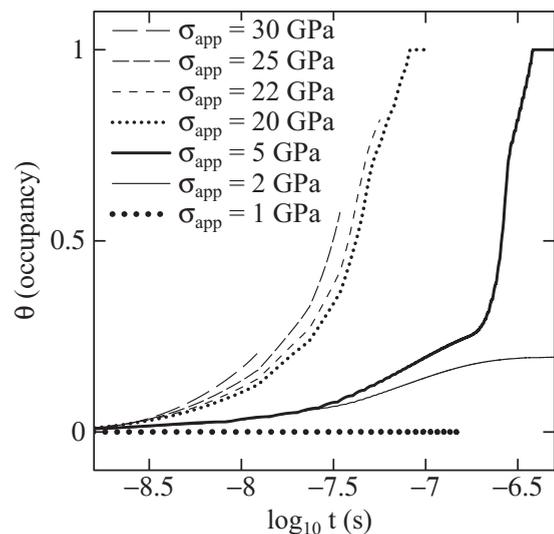
FIG. 8. Evolution of the occupancy θ of hydrogen in the cohesive zone as a function of time, t, for a range of applied stresses σ_{app}. The bulk hydrogen concentration is $C_H = 1$ appm and the relaxation time τ is 10^{-5} s.
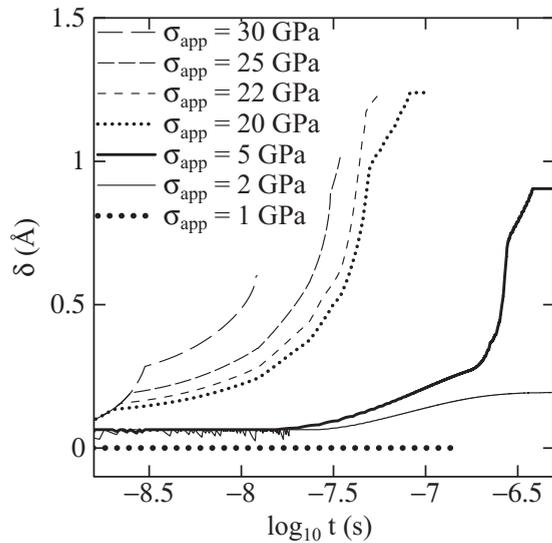
FIG. 9. Evolution of the crack opening, or width δ of the cohesive zone, Fig. 1, as a function of time t for a range of applied stresses, σ_{app}. The bulk hydrogen concentration is $C_H = 1$ appm and the relaxation time τ is 10^{-5} s. Note that for applied stresses of 20 GPa and lower, δ ceases to increase at some time and therefore the crystal does not rupture. In this way see that the cohesive strength of the (111) planes in otherwise perfect α-Fe, in the presence of dissolved hydrogen is greater than 20 GPa.

occupancy by hydrogen θ and the width δ of the cohesive zone as a function of time during the process of following the above steps 1–6 (Sec. II) for a chosen bulk hydrogen concentration of $C_H = 1$ appm and relaxation time, $\tau = 10^{-5}$ s. We observe that as long as the applied stress σ_{app} is greater than 1 GPa then the stress generates a driving force that increases the concentration of hydrogen in the cohesive zone, which in turn leads to an increased crack opening, or separation, which in its turn leads to a reduction in the critical stress σ_{crit}, since as δ increases we move onto traction curves with increasingly smaller maxima (see Fig. 6).

While the integration is quick and has the physical transparency of following the decohesion process in time, there is also the following graphical method to find whether decohesion will occur at a given applied stress. (i) Using the family of traction curves of Fig. 6 find that value of θ (call it θ_c) whose curve shows a maximum at the chosen σ_{app}. (ii) Compare the corresponding cohesive zone chemical potential μ with the bulk μ_b associated with the hydrogen concentration C_H and temperature T. If $\mu_b > \mu$ then the interface will decohere. This is because under this circumstance $\mu \leqslant \mu_b^* \leqslant \mu_b$ at all times. Conversely, if θ_c cannot be attained at the chosen T and σ_{app} then as $t \to \infty$ the interface reaches an equilibrium in which $\mu = \mu_b^* = \mu_b$, the equilibrium θ is smaller than θ_c and decohesion is avoided.

Our procedure (steps 1–6 of Sec. II) allows us to establish a criterion for failure, namely that once the steady state has been reached in the steps 1–6 (Sec. II), we can identify the current critical stress σ_{crit} with the cohesive strength σ_{coh}, and if $\sigma_{app} > \sigma_{coh}$, then the cohesive strength is exceeded and the crystal will rupture across the cohesive zone. We find that in the range $\sigma_{app} = 5$–20 GPa the stress is sufficient to fully
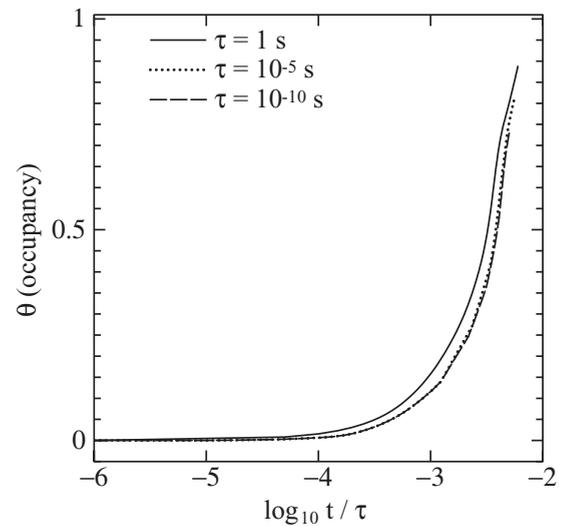
FIG. 10. Evolution of hydrogen occupancy θ of the cohesive zone as a function of time during the decohesion across two (111) crystal planes in α-Fe. Applied stress, $\sigma_{app} = 22$ GPa, bulk hydrogen concentration, $C_H = 1$ appm.

saturate the cohesive zone with hydrogen, $\theta = 1$; only applied stress greater than 20 GPa will exceed the cohesive strength and lead to rupture. The time to rupture depends on the driving force for hydrogen exchange with the bulk and increases with increasing applied stress, σ_{app}. We illustrate this in Figs. 10 and 11 which show the occupancy θ and width δ of the cohesive zone as functions of time. The results we present here are from calculations at a temperature $T = 300$ K. We find that while a change of temperature to 200 K leads to a change in the time to rupture, it does not affect the cohesive strength. We also find that our results are little affected by the bulk hydrogen concentration in the range $C_H = 0.1$–10 appm.
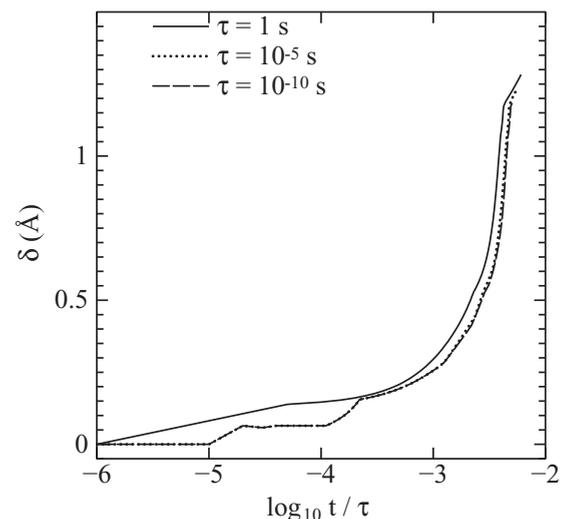
FIG. 11. Evolution of width δ of the cohesive zone as a function of time during the decohesion across two (111) crystal planes in α-Fe. Applied stress, $\sigma_{app} = 22$ GPa, bulk hydrogen concentration, $C_H = 1$ appm.
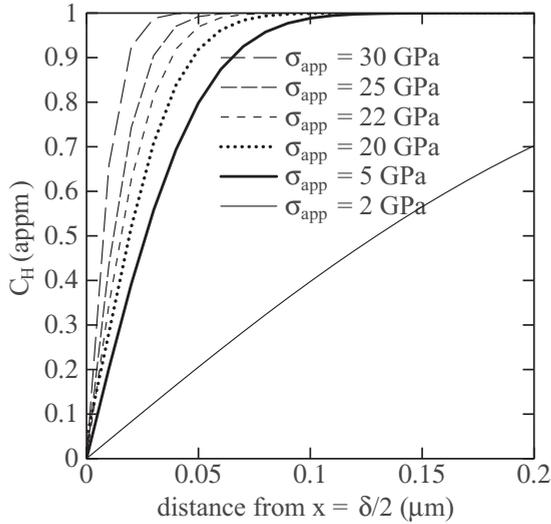
FIG. 12. Hydrogen concentration profiles at the point of rupture or saturation at $T = 300\,\mathrm{K}$ in the bulk for different values of the applied stress σ_{app}. In this case, the bulk hydrogen concentration is $C_{\mathrm{H}} = 1$ appm so that is the value at large distances from the cohesive zone. The distance given is the distance from the boundary, $x = \pm\delta/2$.

Figure 12 shows diffusion profiles between the interface of the cohesive zone with the bulk at $x = \pm\delta/2$ (Fig. 1) at the point of rupture in the case of applied stresses in the interval 22–30 GPa, and at the point of saturation of the cohesive zone for $\sigma_{\mathrm{app}} < 22$ GPa. The effect of hydrogen diffusion into the cohesive zone is to lead to a region in which the hydrogen concentration in the bulk next to the cohesive zone is depleted. The width of this region increases as the applied load decreases.

Van der Van and Ceder [16] discovered in a first principles study of hydrogen affecting the decohesion of (111) planes in aluminum, that there is a Van der Waals phase transition from a dilute cohesive zone (DCZ) to a saturated cohesive zone (SCZ) as the decohesion process proceeds. We see the same phenomenon in the traction curve drawn as a thick solid line in Fig. 6. This line traces the traction curve for decohesion of bulk (111) planes in α-Fe at an applied stress, $\sigma_{\mathrm{app}} = 22$ GPa and with a bulk concentration $C_{\mathrm{H}} = 1$ appm, at 300 K. Initially as the width of the cohesive zone δ increases from zero, the traction curve follows that of pure α-Fe since the occupancy θ is initially close to zero. However, there comes an abrupt, first-order transition to an occupancy close to $\theta = 1$ as indicated by the change to zero slope in the traction curve at $\delta \approx 0.2\,\text{Å}$. Then at $\delta \approx 1.3\,\text{Å}$, the traction curve follows a constant-θ stress-separation curve and since the applied stress, σ_{app}, is in this case greater than the critical stress σ_{crit}, at the maximum of the constant-θ stress-separation curve, the width of the zone continues to increase and the crystal ruptures. On the other hand, if $\sigma_{\mathrm{app}} < \sigma_{\mathrm{coh}}$ as indicated by the dotted line for $\sigma_{\mathrm{app}} = 5$ GPa, again initially the traction curve follows that of pure α-Fe, but while there is again the observed transition from DCZ to SCZ, the crystal does not rupture and the system goes over into an equilibrium state with $\delta \approx 0.9\,\text{Å}$ and $\theta \approx 1$.

The results of this work indicate that very high elastic stresses, in excess of $\sigma_{\mathrm{app}} = 20$ GPa, are required to produce

sufficiently high concentrations of hydrogen in interstitial lattice sites ahead of crack tips and to exceed the critical stress, σ_{crit} (Fig. 6), that results in decohesion (Fig. 9). Whether such stresses can be achieved is debatable. Several approximations due to computational limitations have been made in our investigation of the role of hydrogen during decohesion. One is that we have focused on uniaxial loading. We have neglected possible large shear stresses along the cohesive zone generated by the triaxial state of stress at a crack tip. We do not study plasticity and cleavage phenomena simultaneously so the results of this paper are related only to cleavage. Crack growth also involves nucleation and motion of dislocations along with bond breaking through cleavage. Some dislocation activity may accompany decohesion, and may locally affect stresses at decohesion sites. Dislocation shielding effects ahead of the crack tip can also result in higher tensile stresses. In this paper, we have considered localised decohesion caused by the mobile effect of hydrogen migrating from the bulk to the crack tip. Other possible modes of mass transport involve the crack surfaces behind the crack tip, which serve as an impurity reservoir, or possible hydrogen transport with dislocations that are attracted to the crack tip. We have confined ourselves here to transgranular decohesion ahead of a crack tip. The same approach can be used for studying intergranular fracture. However, the computational costs for a similar study of inter-granular decohesion is significantly higher due to the require-ment of very large supercells to accommodate an explicit grain boundary. Moreover, the structure of the grain boundary admits a much greater complexity of trap sites, which complicates greatly the lattice model (13) for the excess energy.

V. CONCLUSIONS

We have followed previous authors [6,9,16] in describing the process of hydrogen induced decohesion across (111) planes in magnetic α-Fe. The picture is this. At zero applied stress, the hydrogen concentration in tetrahedral sites in between the two (111) planes is essentially zero due to the very low solubility leading to just parts per million levels of hydrogen in the bulk. If a constant traction is applied leading to an applied stress σ_{app} and if the two planes are allowed to decohere by breaking the symmetry of the system, then as they separate the tetrahedral interstices are distorted and enlarged so that they become deeper traps than the bulk sites. This leads to a flux of hydrogen into the cohesive zone, resulting in a reduction in the excess free binding energy of the interface. This in turn leads to an increase in the width δ of the cohesive zone as shown by the family of binding energy curves in Fig. 5. As this process continues, two things may happen; the system may reach an equilibrium state of cohesive zone width δ and hydrogen occupancy θ (which may or may not be saturated, depending on σ_{app}, Fig. 8) or the width will continue to increase until the crystal ruptures revealing two new surfaces having an equilibrium segregation of hydrogen. Rupture is facilitated by the phase transition from a dilute to a saturated cohesive zone as shown in Fig. 6 and as predicted by Van der Ven and Ceder [16].

Our principal conclusion is that the cohesive strength of α-Fe across (111) planes is reduced from 33 GPa (Fig. 6) to 22 GPa due to the presence of dissolved hydrogen in an

otherwise perfect crystal. This value is unaffected by a change in temperature from 300 to 200 K, and is is independent of the bulk hydrogen concentration in the range $C_H = 0.1$–10 appm.

The approach that we outline here is clearly applicable to both intergranular decohesion in α-Fe and interfacial decohesion, for example at the interface with a carbide particle in steel. The interatomic forces in either case are amenable to the tight-binding approximation, so while the problem is greatly complicated by the configuration of trap sites in the cohesive zone, there are no difficulties in principle to extending to microstructures in steels. Such a program of work will provide essential input to continuum finite element models [26], which use "cohesive elements" to represent decohering interfaces and for which the physical basis is still in its infancy.

[1] I. H. Katzarov, D. L. Pashov, and A. T. Paxton, Phys. Rev. Materials **1**, 033602 (2017).

[2] H. Birnbaum, in *Hydrogen Effects on Material Behavior*, edited by N. R. Moody and A. W. Thompson (The Minerals Metals and Materials Society, Warrendale, 1990), pp. 639–660.

[3] Peng Gong and W. M. Rainforth (unpublished).

[4] M. J. Jokl, V. Vitek, and C. J. McMahon Jr., Acta Metall. **28**, 1479 (1980).

[5] J. R. Rice, in *Effect of Hydrogen on Behavior of Materials*, edited by A. W. Thompson and I. M. Bernstein, The Metallurgical Society of AIME (The Metallurgical Society of AIME, New York, 1976), pp. 455–466.

[6] J. P. Hirth and J. R. Rice, Metall. Trans. A **11**, 1501 (1980).

[7] J. R. Rice and J.-S. Wang, Mater. Sci. Eng. A **107**, 23 (1989).

[8] B. R. Lawn, *Fracture of Brittle Solids*, 2nd ed. (Cambridge University Press, Cambridge, UK, 2004).

[9] Y. Mishin, P. Sofronis, and J. Bassani, Acta Mater. **50**, 3609 (2002).

[10] L. Zhong, R. Wu, A. J. Freeman, and G. B. Olson, Phys. Rev. B **62**, 13938 (2000).

[11] W.-T. Geng, A. J. Freeman, G. B. Olson, Y. Tateyama, and T. Ohno, Mater. Trans. JIM **46**, 756 (2005).

[12] Z. X. Tian, J. X. Yan, W. Hao, and W. Xiao, J. Phys.: Condens. Matter **23**, 015501 (2011).

[13] M. Yamaguchi, Metall. Mater. Trans. A **42**, 319 (2011).

[14] M. Yamaguchi, K.-I. Ebihara, M. Itakura, T. Kadoyoshi, T. Suzudo, and H. Kaburaki, Metall. Mater. Trans. A **42**, 330 (2011).

[15] J.-S. Wang, Eng. Fract. Mech. **68**, 647 (2001).

[16] A. Van der Ven and G. Ceder, Acta Mater. **52**, 1223 (2004).

[17] D. Bombac, I. H. Katzarov, D. L. Pashov, and A. T. Paxton, Mater. Sci. Technol. **33**, 1505 (2017).

[18] A. T. Paxton and M. W. Finnis, Phys. Rev. B **77**, 024428 (2008).

[19] A. T. Paxton and C. Elsässer, Phys. Rev. B **82**, 235125 (2010).

[20] A. T. Paxton and C. Elsässer, Phys. Rev. B **87**, 224110 (2013).

[21] J. H. Rose, J. Ferrante, and J. R. Smith, Phys. Rev. Lett. **47**, 675 (1981).

[22] D. de Fontaine, in *Solid State Physics Vol. 47*, edited by H. Ehrenreich and D. Turnbull (Academic Press, San Diego, 1994), pp. 33–176.

[23] J. M. Yeomans, *Statistical Mechanics of Phase Transitions* (Oxford University Press, Oxford, 1993).

[24] A. Ramasubramaniam, M. Itakura, and E. A. Carter, Phys. Rev. B **79**, 174101 (2009).

[25] F. Wang and D. P. Landau, Phys. Rev. Lett. **86**, 2050 (2001).

[26] O. Barrera and A. C. F. Cocks, Philos. Mag. **93**, 2680 (2013).